PHYSICAL REVIEW A VOLUME 44, NUMBER 8 15 OCTOBER 1991

Optimal control of nonlinear classical systems with application to unimolecular dissociation reactions and chaotic potentials

Charles D. Schwieters and Herschel Rabitz
Department of Chemistry, Princeton University, Princeton, New Jersey 08544

(Received 28 January 1991)

In this paper we apply optimal control theory to nonlinear classical systems for the design of electric fields that interact with the systems so that an ensemble of classical trajectories are manipulated in some desired way. Control of selective unimolecular bond dissociation is demonstrated in the classical regime on a model linear triatomic molecule with spreading of the ensemble of trajectories held to a minimum for closer agreement between quantum and classical mechanics. Control was also demonstrated over trajectories in a highly chaotic two-dimensional system. It was found in the cases studied that a high degree of control was attained in situations where the dynamics are chaotic in the absence of a controlling field.

PACS number(s): 03.20.+i, 33.80.Gj, 05.45.+b

I. INTRODUCTION

Recently, it has been proposed that molecular systems be controlled by optimally designed laser pulses [1–9]. Control of vibrational degrees of freedom has been studied theoretically in the harmonic regime [1] where the equations for the optimal field reduce to an analytic form [2–4] and in quantum studies of nonlinear systems [5–7,9]. These studies had in common that the laser pulses were designed to achieve a molecular objective using known dynamical equations, in contrast to previous work in which intuition was used to guide or guess at, typically, a single frequency or simple pulse shape that might achieve the desired result. In this paper we study optimal control of nonlinear vibrational systems described by classical mechanics.

Classical mechanics is frequently used as an approximation of the true quantum mechanics in dynamics calculations of molecular nuclear motion with more than two or three degrees of freedom because the quantum calculations are not currently feasible. In past studies [10–12] quantum and classical dynamics were shown to give similar results for appropriate model systems with one or two degrees of freedom. Even when the expectation values of the quantum wave packet did not exactly correspond to the averages over the classical trajectories, observables such as asymptotic dissociation probabilities were quite similar [10,11]. Notable exceptions to quantum-classical agreement were seen to occur because of differences between quantum and classical resonances, due to wave-packet spreading and due to quantum effects such as tunneling [12]. However, circumstances that foster these discrepancies appear to be reasonably well understood and perhaps can be avoided in a design scenario.

Hence, the desire to optimally achieve unimolecular chemical reactions in large molecules by means of shaped laser pulses leads to the need for designing electric fields to manipulate classical models of the molecules using optimal control theory. In addition to achieving a molecular objective, one might be able to steer the classical trajectories away from regions of phase space where quantum-classical differences would be likely to appear. Moreover, control of nonlinear classical systems is important in its own right because the macroscopic world is well described by classical mechanics. Control of such systems is now an active field of research [13–15]. Dynamical chaos is evident in many nonlinear systems in classical mechanics and presents problems for "control" of these systems: if a bundle of trajectories that is initially localized spreads throughout phase space, an average of position or momentum over the trajectories cannot be said to have been acceptably controlled due to the large variance. We address this problem by weighting against such spread in the field design process.

In this paper, we explore the use of optimal control theory for controlling systems modeling molecular vibrational degrees of freedom in the absence of rotation. In Sec. II we present the optimal control formalism used. In Sec. III, we show results for control of a system modeling unimolecular dissociation, and in Sec. IV we examine the results for control in a system having a highly chaotic potential. Section V contains a brief conclusion.

II. CONTROL FORMALISM

In this section we present a cost functional that is minimized with respect to the form of the applied electric field so that a molecular objective may be met. The cost functional contains terms for each property we wish to achieve in the design process. In addition, we require that Hamilton's equations be obeyed. The Hamiltonian for our system can be written as

$$H_T = H_0 + H_I \ , \tag{2.1}$$

where H_0 is the field free Hamiltonian and H_I represents the molecule-laser interaction energy, which, in the dipole approximation, can be written as

$$H_I = -\mathbf{D}(\mathbf{q})\cdot\boldsymbol{\epsilon}(t) \ . \tag{2.2}$$

Here $\mathbf{D}$ is the dipole moment function, $\boldsymbol{\epsilon}(t)$ is the electric field, and $\mathbf{q}$ are the displacements from equilibrium of each coordinate in the molecule (bond stretch, angle displacement, etc.). We will take $\boldsymbol{\epsilon}(t)$ to be polarized along $\mathbf{D}$ for the remainder of this paper. H_0 can be written as

$$H_0 = \tfrac{1}{2}\mathbf{p}^{\mathrm{T}}\underline{G}\mathbf{p} + V(\mathbf{q}) \ , \tag{2.3}$$

where $\mathbf{p}$ are the momenta conjugate to $\mathbf{q}$, $\underline{G}$ is the Wilson G matrix [16] with units of inverse mass, and $V(\mathbf{q})$ is the potential-energy function.

In order to achieve the molecular objective, we introduce a cost functional

$$J = \Phi[\mathbf{z}(T)] + \int_0^T dt\{L_1[\mathbf{z}(t)] + L_2[\epsilon(t)]\} \ , \tag{2.4}$$

where Φ is an error function that guides the state $\mathbf{z}^T = (\mathbf{q}^T, \mathbf{p}^T)$ to some specified objective at the target time T. L_1 is the cost of $\mathbf{z}$ sampling undesired regions of phase space during the pumping interval $[0,T]$. For instance, it might be desirable that the energy of the molecule be small during the control interval. L_2 is the cost for the electric field having undesirable properties, such as being too complicated or too large in magnitude to create in the laboratory, etc.

The constraint of Hamilton's equations of motion

$$\dot{\mathbf{z}} = \begin{bmatrix} \underline{G}\mathbf{p} \\ -\partial H_T/\partial\mathbf{q} \end{bmatrix} = f(\mathbf{z},\epsilon) \tag{2.5}$$

being satisfied can be included in the minimization process by introducing a Lagrange multiplier vector $\underline{\lambda}$:

$$\bar{J} = J - \int_0^T dt\,\underline{\lambda}^T(t)[\dot{\mathbf{z}}(t) - f(\mathbf{z},\epsilon)] \ . \tag{2.6}$$

By introducing infinitesimal variations $\epsilon(t)\rightarrow\epsilon(t)+\delta\epsilon(t)$ and $\mathbf{z}\rightarrow\mathbf{z}(t)+\delta\mathbf{z}(t)$, one obtains

$$\begin{aligned} \delta\bar{J} = {} & \frac{\partial\Phi[\mathbf{z}(T)]}{\partial\mathbf{z}}\delta\mathbf{z}(T) \\ & + \int_0^T dt \left[\frac{\partial L_1[\mathbf{z}(t)]}{\partial\mathbf{z}}\delta\mathbf{z}(t) + \frac{\partial L_2[\epsilon(t)]}{\partial\epsilon}\delta\epsilon(t) \right] \\ & - \int_0^T dt\,\underline{\lambda}^T(t) \left[\delta\dot{\mathbf{z}}(t) - \frac{\partial f}{\partial z}\delta\mathbf{z}(t) - \frac{\partial f}{\partial\epsilon}\delta\epsilon(t) \right] \ . \end{aligned} \tag{2.7}$$

Integrating by parts and rearranging, we obtain

$$\begin{aligned} \delta\bar{J} = {} & \left[\frac{\partial\Phi}{\partial\mathbf{z}} - \underline{\lambda}^T(T) \right]\delta\mathbf{z}(T) \\ & + \int_0^T dt \left[\dot{\underline{\lambda}}^T(t) + \frac{\partial L_1}{\partial\mathbf{z}} + \frac{\partial f}{\partial\mathbf{z}} \right]\delta\mathbf{z}(t) \\ & + \int_0^T dt \left[\frac{\partial L_2}{\partial\epsilon} + \underline{\lambda}^T(T)\frac{\partial f}{\partial\epsilon} \right]\delta\epsilon(t) \ . \end{aligned} \tag{2.8}$$

If we choose the Lagrange multipliers to obey the equation

$$\dot{\underline{\lambda}}^T = -\frac{\partial L_1}{\partial\mathbf{z}} - \underline{\lambda}^T\frac{\partial f}{\partial\mathbf{z}} \tag{2.9}$$

with the final condition $\underline{\lambda}^T(T) = \partial\Phi/\partial\mathbf{z}$, then the change in the augmented cost functional due to a change in field reduce to

$$\delta\bar{J} = \int_0^T dt \left[\frac{\partial L_2}{\partial\epsilon} + \underline{\lambda}^T\frac{\partial f}{\partial\epsilon} \right]\delta\epsilon(t) \ , \tag{2.10}$$

and the gradient of $\bar{J}$ with respect to the field can be written as

$$\frac{\delta\bar{J}}{\delta\epsilon(t)} = \frac{\partial L_2}{\partial\epsilon} + \underline{\lambda}^T(t)\frac{\partial f}{\partial\epsilon} \ . \tag{2.11}$$

To solve for the field that gives minimal cost, $\epsilon(t)$ is first discretized over the time interval $[0,T]$. An initial guess for the field is made and the equations of motion for the state (2.5) can be integrated forward in time. Once $\mathbf{z}(T)$ is obtained, (2.9) can be integrated backwards in time to solve for the Lagrange multipliers. One can then calculate the gradient of $\bar{J}$ with respect to the guessed field, and an updated field that gives lower cost can be obtained by minimization techniques such as steepest descent, conjugate gradient, or Newton's method. This overall procedure is repeated until the norm of the gradient is smaller than some prescribed value or until the cost does not significantly decrease in successive iterations. For the results in this paper we used the same conjugate gradient routine as employed in Ref. [1]. Definitions of the details of the Hamiltonian and the cost functional will be stated in the next two sections prior to showing results for individual systems.

III. UNIMOLECULAR BOND BREAKING

In this section we present results for a classical system modeling selective unimolecular dissociation. The system treated in this section is the same as that studied quantum mechanically in Ref. [6] and the results here are compared to those of the previous study.

The system chosen for proof of principle was a model A-B-C linear molecule. The G matrix is taken as

$$\underline{G} = \begin{bmatrix} 1/\mu_1 & -1/M_B \\ -1/M_B & 1/\mu_2 \end{bmatrix} , \tag{3.1}$$

where $1/\mu_1 = 1/M_A + 1/M_B$, $1/\mu_2 = 1/M_B + 1/M_C$, $M_A = 18.998$ amu, $M_B = 12.011$ amu, and $M_C = 35.453$ amu. The potential is described by two Morse oscillators:

$$V = D_1[1-\exp(-\alpha_1 q_1)]^2 + D_2[1-\exp(-\alpha_2 q_2)]^2 \ , \tag{3.2}$$

where q_1 is the displacement of the $A-B$ bond from its equilibrium position and q_2 is the displacement of the $B-C$ bond. The parameters for (3.2) are

$D_1 = 0.1976$ a.u. $= 5.376$ eV ,

$D_2 = 0.1371$ a.u. $= 3.730$ eV ,

$\alpha_1 = 0.9217$ a.u. $= 0.4877$ Å^{-1} ,

$\alpha_2 = 1.0273$ a.u $= 0.5436$ Å^{-1} , and the harmonic frequencies are fairly close: $\omega_1^0=1098$ cm^{-1}, $\omega_2^0=923$ cm^{-1}. The only interaction between the two bond stretches is through a kinetic coupling term $-p_1p_2/M_B$.

The dipole function was taken as

$$D(q_1,q_2)=A[(q_0+q_1)\exp(-\beta q_1)-(q_0+q_2)\exp(-\beta q_2)]\ , \qquad (3.3)$$

where $A=1$ D$=0.3934$ a.u., $\beta=1$ a.u., and $q_0=2$ a.u., so that the dipole is equal in magnitude but opposite in sign for the two degrees of freedom. This choice for dipole function is somewhat unusual because the equilibrium position is past the peak in the dipole function (the peak occurs at -1 a.u.). For all the cases shown here, the electric field is polarized along the molecular dipole.

Initial conditions were chosen in a position space grid about the minimum of the potential function and were weighted by the Wigner function[17] for the ground state of a two-dimensional harmonic oscillator:

$$\Gamma(q_1,q_2,p_1,p_2)=K\exp(-a_1\tilde{q}_1^2-a_2\tilde{q}_2^2-a_3\tilde{p}_1^2-a_4\tilde{p}_2^2)\ , \qquad (3.4)$$

where $a_1=\tilde{\omega}_1/\hbar$, $a_2=\tilde{\omega}_2/\hbar$, $a_3=(a_1\hbar)^{-1}$, $a_4=(a_2\hbar)^{-1}$, and K is a normalizing factor. $\tilde{q}_i(q_1,q_2)$ and $\tilde{p}_i(p_1,p_2)$ are the normal coordinates at the equilibrium position and corresponding conjugate momenta, and $\tilde{\omega}_i$ are the eigenfrequencies. For our model system, the Wigner distribution is very strongly peaked about zero in the momenta, so all the initial conditions were chosen with $p_1=p_2=0$. Our results were found to converge using 400 classical trajectories.

It should be noted that computer memory requirements for this optimization procedure are much more restrictive than in pure trajectory calculations. In normal trajectory calculations each trajectory can be integrated separately and desired information stored. The forward integration for optimal control calculations is the same, but the calculation of each Lagrange multiplier depends on all the other multipliers *and* all of the trajectories simultaneously.

In the previous quantum study of this system the objective was to break the $A-B$ bond with minimal disturbance of the $B-C$ bond and minimal electric-field fluence. Hence, the elements of the cost functional were chosen as follows:

$$\Phi[\mathbf{z}(T)]=\tfrac{1}{2}[\langle q_1(T)\rangle-\gamma]^2P_{f1}+\tfrac{1}{2}\langle p_1(T)\rangle^2h[-\langle p_1(T)\rangle]P_{f3}\ , \qquad (3.5a)$$

where $\langle q_1(T)\rangle$ and $\langle p_1(T)\rangle$ are the quantum-mechanical expectation values of position and momentum of the $A-B$, bond γ is the target stretch of the $A-B$, bond, P_{f1} and P_{f3} are weighting factors, and $h(x)$ is the Heaviside function

$$h(x)=\begin{cases}1 & \text{if } x\geq 0\\ 0 & \text{if } x<0\end{cases}$$

so that $\langle p_1\rangle$ will be positive at the final time and atom A is moving away from atom B. L_1 was taken as

$$L_1=\tfrac{1}{2}[\langle q_2(t)\rangle-\langle q_2(0)\rangle]^2W_2+\tfrac{1}{2}[\langle p_2(t)\rangle-\langle p_2(0)\rangle]^2W_4\ , \qquad (3.5b)$$

where W_2 and W_4 are weighting factors. This term weights against excess excitation of the $B-C$ bond away from its equilibrium position and momentum. Finally, L_2 was chosen to be

$$L_2=\tfrac{1}{2}\omega_e\epsilon^2(t)\ , \qquad (3.5c)$$

where ω_e is the weight of this term. When integrated over the interval $[0,T]$ this term represents the fluence of the electric field.

As a starting point for the classical study, we integrated the classical equations of motion with the electric field obtained from the quantum-mechanical optimal control calculation reported elsewhere [6]. The results are shown in Fig. 1 and were checked by integrating backwards. Figure 1(a) shows the electric field which is shaped almost sinusoidally during the control interval $0\leq t\leq T=0.1$ ps. The two systems (quantal and classical) were then integrated for an additional 0.05 ps under zero field after the pulse had ended to better see the fate of the molecule. Figures 1(b) and 1(c) compare the quantum expectation values of position and momentum to averages over the classical trajectories of the analogous quantities. Figure 1(d) is a plot of the average value of the bond energies defined as

$$e_i=\frac{p_i^2}{2\mu_i}+D_i[1-\exp(-\alpha_iq_i)]^2 \qquad (3.6)$$

for the $A-B$ and $B-C$ bonds. One can see that the dynamics are virtually identical for the first 0.04 ps, and thereafter they differ. The onset of large spreading of both the quantum wave packet and of the ensemble of classical trajectories occurs at about 0.04 ps, so it is understandable that the two types of dynamics should differ. However, the trends in displacement, momentum, and energy are quite similar: the stretch of q_1 remains larger than that of q_2, and the momentum of the $A-B$ bond is positive in both the quantal and the classical results. Figure 1(d) shows that the energy remains larger in the target bond for both the quantum and classical calculations, and both appear very close to the dissociation energy of the $A-B$ bond (0.1986 a.u.) at 0.05 ps after the field has turned off. By projecting the final quantum wave packet on the asymptotic scattering states, it was determined that 51% dissociated into the target channel, and virtually all of the remaining 49% of the $A-B$-C molecules were left excited but undissociated in either channel [6]. The corresponding classical calculation yielded a similar result of 60% in the target channel, but 35% went into the undesired products $A-B+C$ and $A+B+C$.

Now we will explore the process of calculating optimal fields using classical mechanics directly. Ultimately, such fields should be inserted into Schrödinger's equation for their quantum action as well. The latter quantum control calculations will not be part of the present work, but

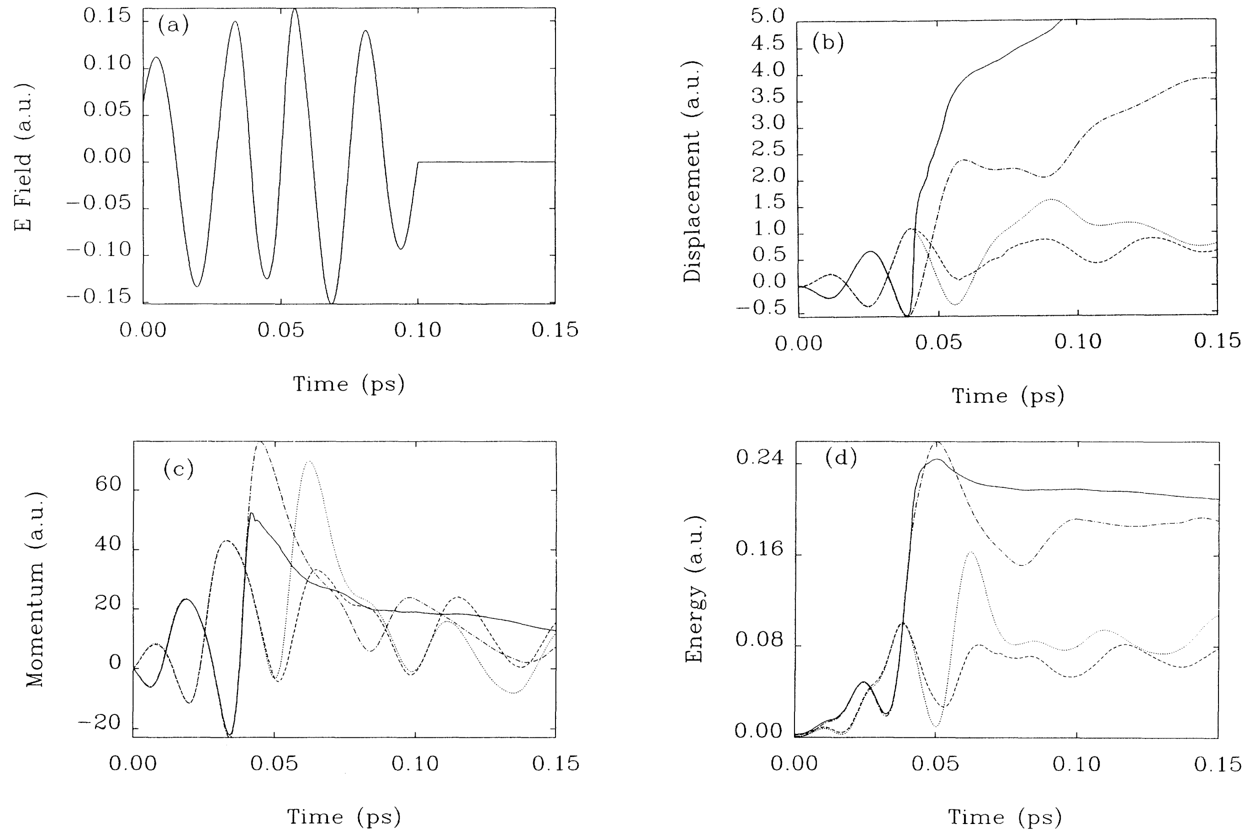

FIG. 1. Comparison of quantum and classical expectation values under the effect of the electric field in (a). Panel (b) compares displacement of $\langle q_1 \rangle$ and $\langle q_2 \rangle$. Panel (c) compares the conjugate momenta and (d) shows the comparison of bond energy defined in Eq. (3.6). Solid lines denote quantum results for bond 1, dashed lines denote quantum results for bond 2, dash-dotted lines denote classical results for bond 1, and dotted lines show classical results for bond 2. These results show that, while the specifics of the dynamics differ, the trends are similar.

some logic relevant to them will be discussed in the present classical control studies. Initially, we used the same internal coordinates for the classical calculation as were used for the previous quantum results, but it soon became apparent that, although the control calculations could be performed, the system ended up in the wrong exit channel due to the kinetic coupling term in the Hamiltonian. The energy would be localized in the $A-B$ bond at the target time, with the $A-B$ bond stretched and its momentum positive. However, integration beyond the target time revealed that the energy transferred to the $B-C$ bond shortly after T due to the $-p_1 p_2/M_B$ term in the Hamiltonian.

To ameliorate this situation, we transformed to scattering coordinates

$$Q_1=q_1+M_C/(M_B+M_C)q_2\ , \tag{3.7}$$

$$Q_2=q_2\ , \tag{3.8}$$

$$P_1=p_1\ , \tag{3.9}$$

$$P_2=p_2-M_C/(M_B+M_C)p_1\ , \tag{3.10}$$

where Q_1 is the displacement from equilibrium of the center of mass of the B-C diatom from the A atom and Q_2 is the displacement from equilibrium of the $B-C$ bond. The Hamiltonian in this new coordinate system is then written as

$$H_0=\frac{1}{2}\left[\frac{P_1^2}{M_1}+\frac{P_2^2}{M_2}\right]+D_1\{1-\exp[-\alpha_1(Q_1-\zeta Q_2)]\}^2$$
$$+D_2[1-\exp(-\alpha_2 Q_2)]^2\ , \tag{3.11}$$

where $M_1=[M_A(M_B+M_C)]/(M_A+M_B+M_C)$, $M_2=(M_B M_C)/(M_B+M_C)$, $\zeta=M_C/(M_B+M_C)$, and

$$H_I=A\{(q_0+Q_2)\exp(-\beta Q_2)$$
$$-(q_0+Q_1-\zeta Q_2)\exp[-\beta(Q_1-\zeta Q_2)]\}\epsilon(t)\ . \tag{3.12}$$

In this coordinate system there is no momentum coupling—the cross terms have been moved to the potential and dipole functions. Here we can specify the target state more readily because the desired goal is to stretch Q_1, the distance between the A atom and the remaining B-C diatom. Since the dynamics are the same regardless of the coordinate system, in principal, we could have just transformed the cost functional to have achieved the same results. However, this transformation would have introduced nonintuitive cross terms into the cost functional and it would have lost easy physical interpretation.

Initially, we used a cost functional with the following terms:

$$\Phi[\mathbf{z}(T)]=\tfrac{1}{2}[\bar{Q}_1(T)-\gamma]^2P_{f1}+\tfrac{1}{2}\bar{P}_1^{\,2}(T)h[-\bar{P}_1(T)]P_{f3}\ , \qquad (3.13a)$$

$$L_1=\tfrac{1}{2}[\bar{Q}_2(t)-\bar{Q}_2(0)]^2W_2+\tfrac{1}{2}[\bar{P}_2(t)-\bar{P}_2(0)]^2W_4\ , \qquad (3.13b)$$

$$L_2=\tfrac{1}{2}\omega_e\epsilon^2(t)\ , \qquad (3.13c)$$

where the bars over $\bar{Q}_i$ and $\bar{P}_i$, $j=1,2$ denote averages over the trajectories weighted by the value of the Wigner function evaluated at their initial conditions, e.g.,

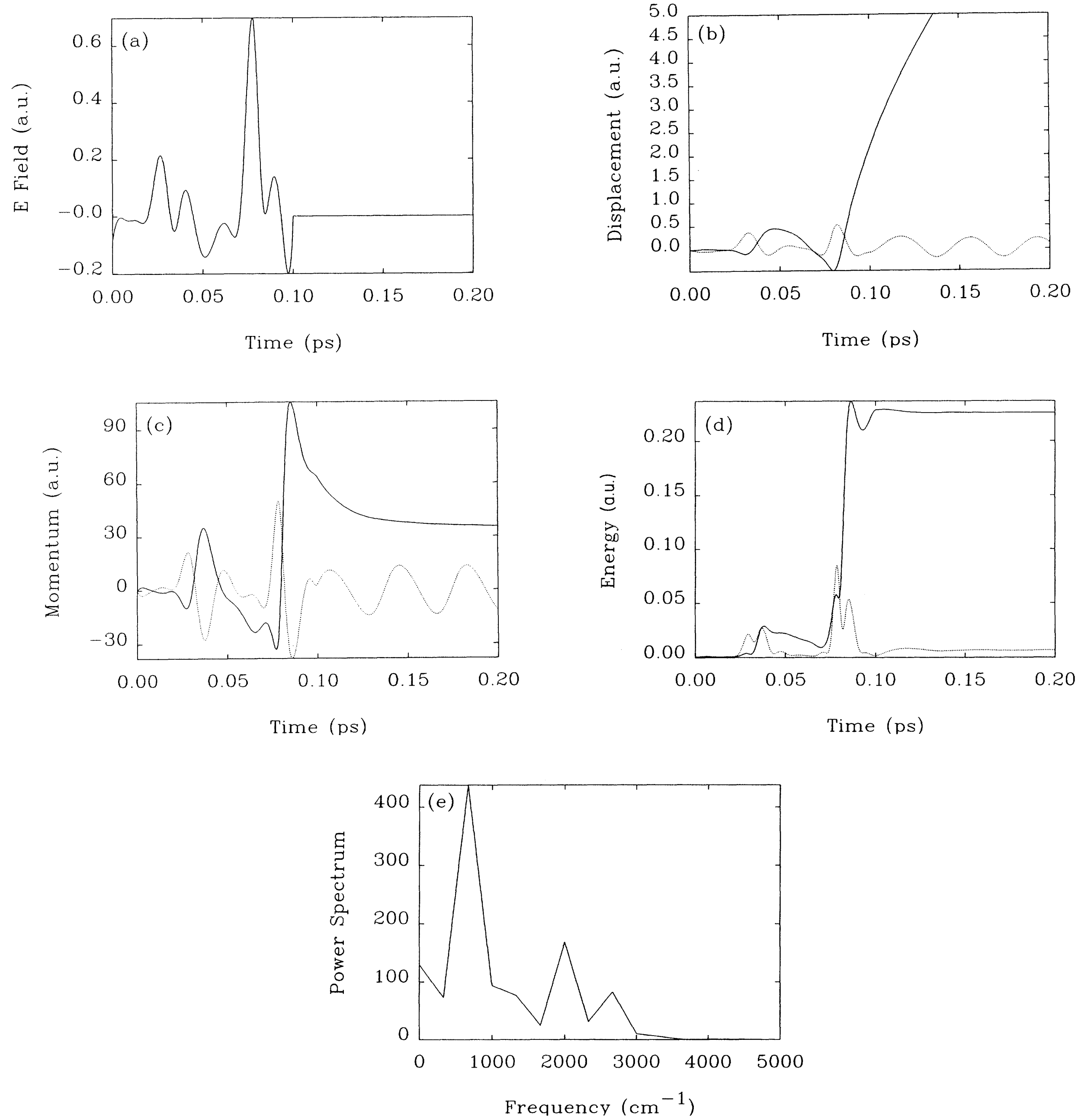

FIG. 2. Optimal control using scattering coordinates: (a) the electric field for the control interval up to 0.1 ps. Also shown are zero-field results for an additional 0.1 ps. Panel (b) is the displacement of Q_1 shown as a solid line and Q_2 shown as a dotted line, while panel (c) shows the conjugate momenta. Panel (d) shows bond energies as defined in Eq. (3.16). These plots show that the stronger bond, described asymptotically by Q_2, is selectively excited, ultimately leading to its preferential dissociation. Panel (e) is the power spectrum of the field shown in (a).

$$\bar{Q}_1(t)=\sum_{i=1}^{N}\Gamma[Q_{1i}(0),Q_{2i}(0),P_{1i}(0),P_{2i}(0)]Q_{1i}(t)\ . \tag{3.14}$$

Here the index i refers to the ith initial condition out of a total of N. This cost functional is just the classical analog of the quantum cost functional (3.5a) with the exception that the coordinate system has been changed.

Armed with the knowledge that quantum and classical mechanics differ as the wave packet or initial bundle of classical trajectories spreads, we sought to minimize this cause of discrepancy by including variance terms in the cost functional. The hope is that if the variance of the classical trajectories could be kept small over the control interval, the spread of the quantum wave packet might also be small, thereby reducing one cause for classical-quantal differences. Therefore, we added the following terms to the cost functional:

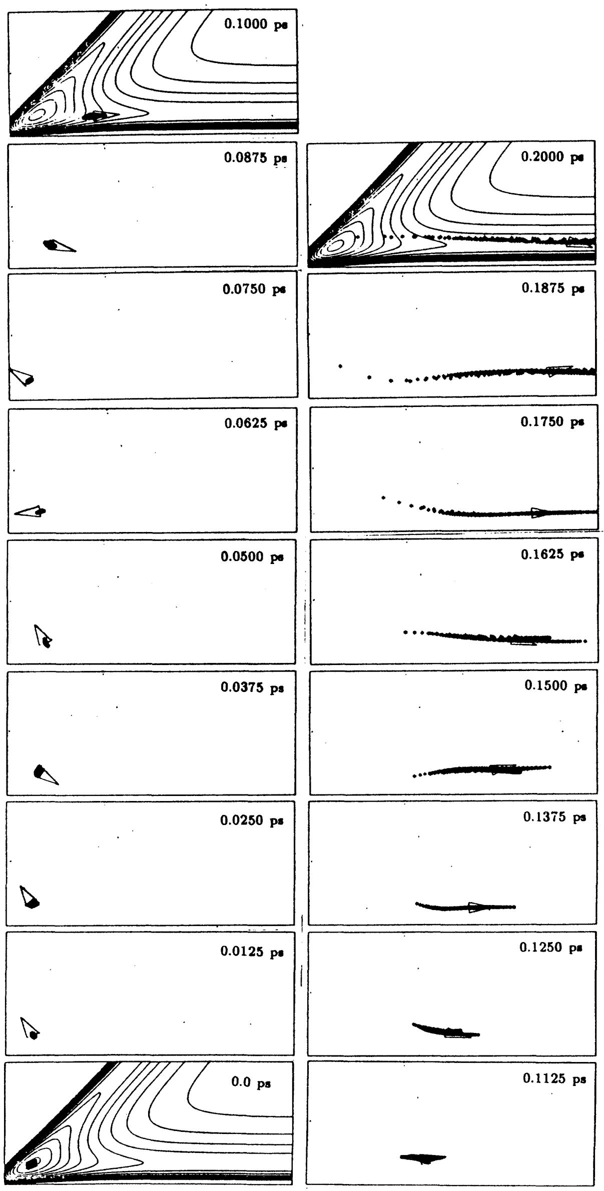

FIG. 3. Snapshots of the trajectories for the case in Fig. 2 are shown here with triangles at the mean position showing the direction (not magnitude) of the mean value of momentum. The snapshots are at intervals of 0.0125 ps and show that most trajectories are heading out the target coordinate. Potential-energy contours are shown at $t=0$, $t=T$, and $t=0.2$ ps.

$$\Phi'[\mathbf{z}(T)]=\Phi[\mathbf{z}(T)]+\tfrac{1}{2}P_{V1}\sum_{i=1}^{N}\Gamma_i[Q_{1i}(T)-\bar{Q}_1(T)]^2 +\tfrac{1}{2}P_{V2}\sum_{i=1}^{N}\Gamma_i[Q_{2i}(T)-\bar{Q}_2(T)]^2\ , \tag{3.15a}$$

$$L_1'=L_1[\mathbf{z}(T)]+\tfrac{1}{2}W_{V1}\sum_{i=1}^{N}\Gamma_i[Q_{1i}(t)-\bar{Q}_1(t)]^2 +\tfrac{1}{2}W_{V2}\sum_{i=1}^{N}\Gamma_i[Q_{2i}(t)-\bar{Q}_2(T)]^2\ , \tag{3.15b}$$

where P_{V1}, P_{V2}, W_{V1}, and W_{V2} are weighting factors (the subscript V denotes variance), and Γ_1 refers to the value of the Wigner distribution for the ith initial condition. Φ' adds a cost for variance in position space at the target time, while L_1' adds a cost for the variance of Q_1 and Q_2 over the entire control interval. The variances of the momenta could also be added to the cost functional, but were not included in this study.

A sample of the results from optimal control of the classical A-B-C system can be seen in Figs. 2 and 3. For the results, the weighting factors were $P_{f1}=1.60\times10^4$, $P_{f3}=3.54$, $P_{V1}=4.73\times10^6$, $W_2=2.38\times10^5$, $\omega_e=2.867$, and all others were set equal to zero. These weight factors were used for calculations done in atomic units. The target time was 0.1 ps.

The electric field is shown in Figs. 2(a). It is seen to have more structure than the quantum result in Fig. 1(a), but this may largely be due to the different cost functional used. The pulse is dominated by the large peak at $t=0.075$ ps with a peak value of about 0.7 a.u.$=4\times10^{11}$ V/m. The power spectrum of this pulse is shown in Fig. 2(e). The primary peak is at about 700 cm^{-1}, shifted well to the red of either of the fundamental frequencies of the system. Also present are overtone frequencies at 2000 and 2700 cm^{-1} and a non-negligible dc component.

The result of applying this field to the system can be seen in Figs. 2(b)–2(d). The average displacement of the target coordinate $\bar{Q}_1$ is seen in Fig. 2(b) to rise monotonically after the target time, while $\bar{Q}_2$ oscillates in a bound fashion. In Fig. 2(c), the average momentum of the target coordinate $\bar{P}_1$ is seen to peak at 0.085 ps immediately following the large peak in the electric field. $\bar{P}_1$ then steadily decreases as the bundle of trajectories climbs out of the well into the target channel. The target momentum remains positive asymptotically, showing that the trajectories are moving away from the region where A and $B-C$ interact. As expected, the momentum of the B-C bond oscillates 90° out of phase of its displacement after the field is turned off. We now redefine the bond energy as

$$e_i=\tfrac{1}{2}P_i^2/M_i+D_i[1-\exp(-\alpha_i Q_i)]^2 \tag{3.16}$$

for the two degrees of freedom ($i=1,2$), and their values averaged over all trajectories are shown in Fig. 2(d). The energy averaged over the trajectories for the target bond at the target time is well above the 0.1976 a.u. required for dissociation, while the $B-C$ bond has very little energy at the target time and its peak value is about 0.08 a.u., well below the 0.137 a.u. required for dissociation of this bond.

Figure 3 shows snapshots of the trajectories at regular times over the interval [0,0.2 ps]. The triangular arrowheads emanating from the mean position of the trajectory bundle indicate the direction of the average momentum. One can see that the trajectories do not spread much before the target time of 0.1 ps, but do start spreading significantly after this time along the target coordinate due to differences in the momenta of the trajectories (re-

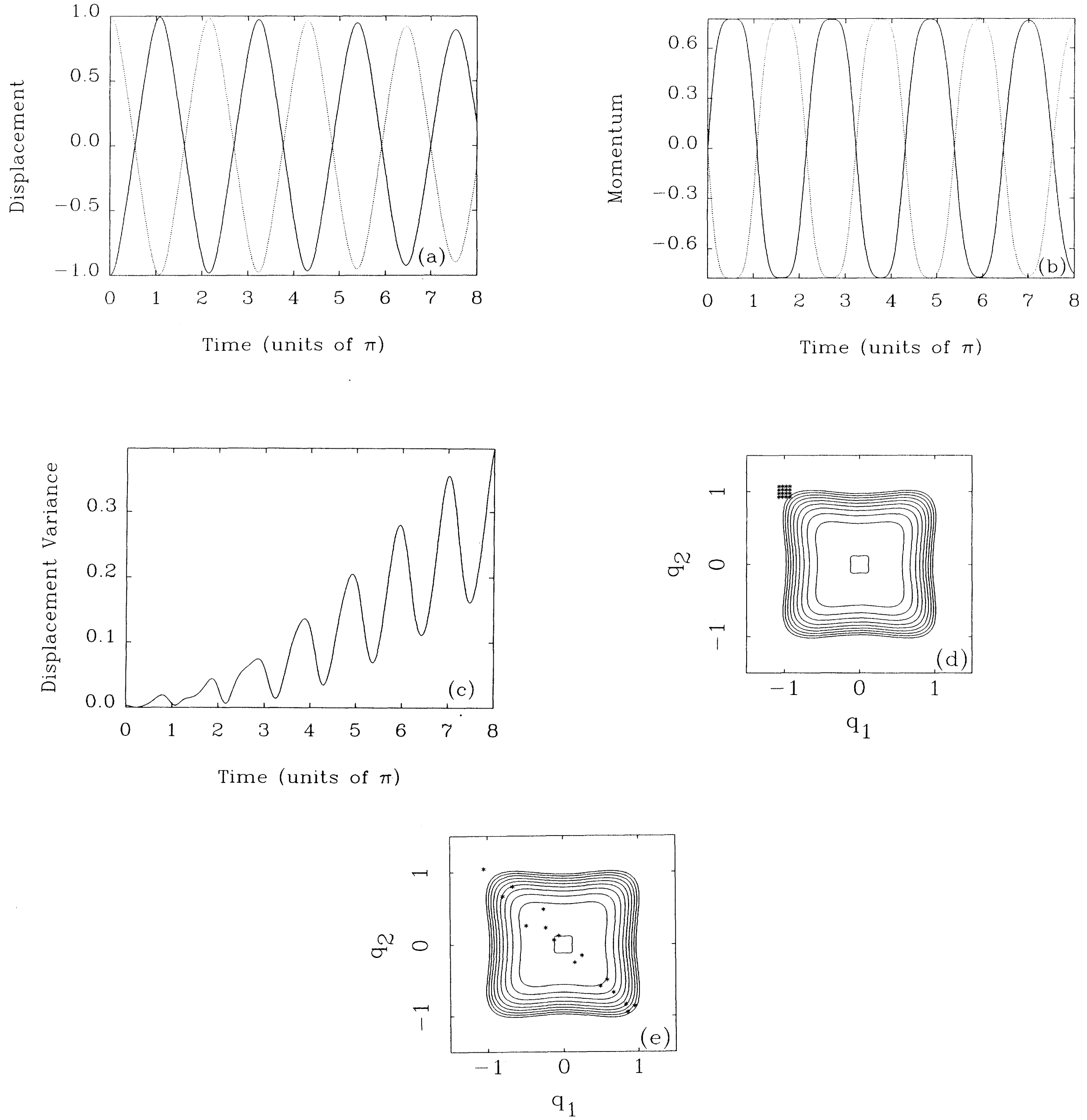

FIG. 4. Integration of trajectories under zero field for initial conditions clustered around $q_1=-1$, $q_2=1$ for $k=0.4$: (a) displacement, (b) momentum, (c) displacement variance, (d) trajectories at $t=0$, and (e) the trajectories at $t=8\pi$. Properties of coordinate 1 are shown as solid lines and those of coordinate 2 are shown as dotted lines. All units are dimensionless.

call that momentum variance was not included in the cost functional). It can be seen that the large peak in the electric field at 0.085 ps slams the bundle into a repulsive wall. The bundle then departs from the wall with large momentum and heads out the target channel.

The equations of motion for the 400 trajectories were integrated for 2.0 ps after the target time to find asymptotic product distributions. We found that 96.5% achieved the desired goal of leaving the interaction region with the $A-B$ bond broken, but with $B-C$ still bound. 3.1% remained with A-B-C still fully bound, while 0.4% had broken the $B-C$ bond and left the $A-B$ bond intact, and none of the trajectories had dissociated both bonds. These results show high specificity for breaking the target bond, which, in this case, is 30% stronger than the non-target bond.

IV. CONTROL ON A CHAOTIC POTENTIAL SURFACE

In this section, we present control results for the highly chaotic bound system

$$H_0=\tfrac{1}{2}(p_1^2+p_2^2+q_1^4+q_2^4)-kq_1^2q_2^2 \tag{4.1}$$

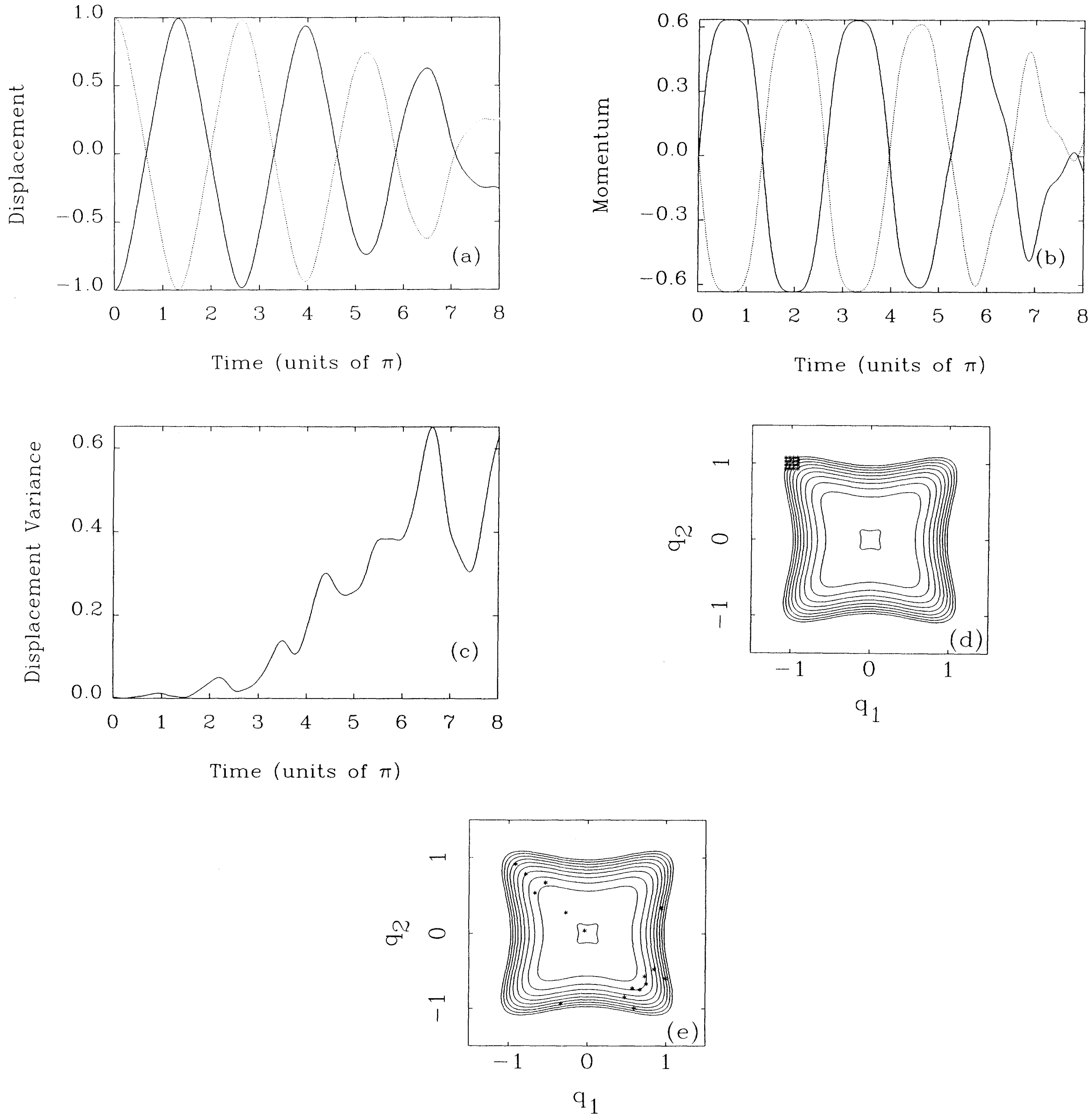

FIG. 5. Integration of trajectories under zero field for initial conditions clustered around $q_1=-1$, $q_2=1$ for $k=0.6$; (a) displacement, (b) momentum, (c) displacement variance, (d) trajectories at $t=0$, and (e) the trajectories at $t=8\pi$. Properties of coordinate 1 are shown as solid lines and those of coordinate 2 are shown as dotted lines. All units are dimensionless.

studied in Ref. [18]. This potential has the property that motion at any energy can be determined from the motion for $E=1$ by simple scaling relations [19]. Accordingly, the fraction of energy allowed phase space filled with irregular trajectories is invariant to energy and depends only on the coupling parameter k. It has been shown [18] that the energy shell phase space is entirely filled for $k \geq 0.6$. We chose this potential because of the property that irregular motion is not limited to narrow energy regions, as is the case, for example, with the Hénon-Heiles potential [20]. Irregular trajectories have the property that small errors in initial position grow exponentially asymptotically and this property presents problems for controlling the motion of trajectories with slightly different initial conditions.

We chose to attempt to control mean values of an ensemble of classical trajectories with the initial conditions clumped closely on this surface for $k=0.4$, where irregular trajectories fill about 90% of available phase space, and for the completely chaotic case $k=0.6$. To influence the motion on the potential surface, we chose the interaction Hamiltonian to be

$$H_I = q_1 \epsilon(t) \; , \tag{4.2}$$

so that only q_1 can be directly manipulated by the driving field. Since all of our targets involved q_2, this choice for H_I makes control even more challenging.

The goal in these calculations was to see to what extent the state averaged over initial conditions could be controlled and the spread of trajectories minimized for two basic starting conditions: (1) high energy with the target also at a high energy, and (2) starting at low energy and preferentially pumping one degree of freedom to a large displacement. The cost functional used was

$$\begin{aligned} 2J = {} & [\bar{\mathbf{z}}(T)-\gamma]^T \underline{P}_f [\bar{\mathbf{z}}(T)-\gamma] \\ & + \int_0^T dt [\bar{\mathbf{z}}^T(t) \underline{W} \bar{\mathbf{z}}(t) + \omega_e \epsilon^2(t)] \\ & + \sum_{i=1}^{N} \sum_{j=1}^{4} P_{Vj} \Gamma_i [z_{i,j}(T) - \bar{z}_j(T)]^2 \\ & + \int_0^T dt \sum_{i=1}^{N} \sum_{j=1}^{4} W_{Vj} \Gamma_i [z_{i,j}(t) - \bar{z}_j(t)]^2 \; , \end{aligned} \tag{4.3}$$

where the first term is a quadratic cost for the mean of the state not hitting the target γ at the target time T, the second term is a cost for mean values of position, momentum, and field being nonzero, and the last two terms weight against variance at the target time and during the control interval, respectively. $\underline{P}_f$ and $\underline{W}$ are 4×4 diago-

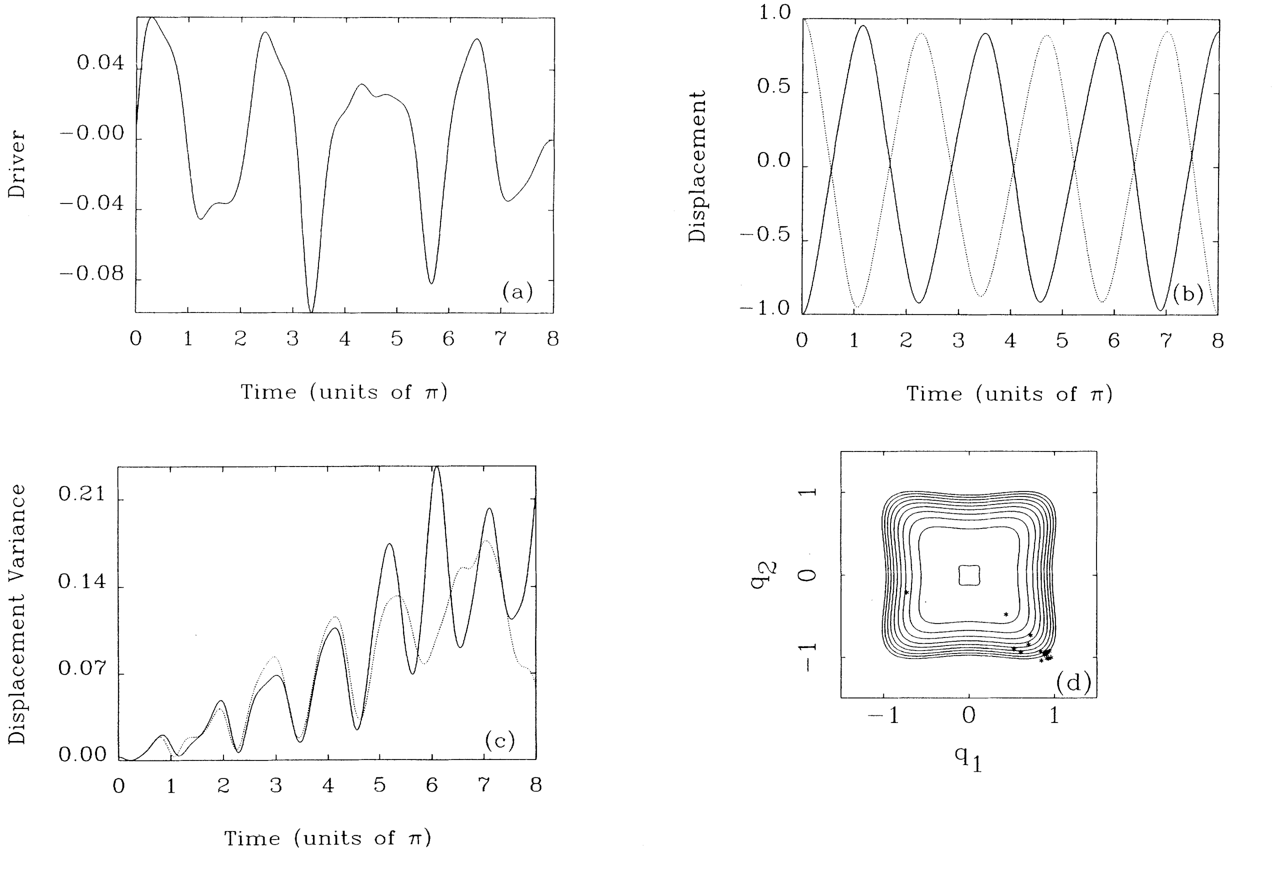

FIG. 6. Optimal control results for the system shown in Fig. 4 with no variance control: (a) optimal field, (b) displacement, (c) displacement variance, and (d) the trajectories at the final time. The objective of stretching $\bar{q}_2$ to 1 was met with some spreading. Properties of coordinate 1 are shown as solid lines and those of coordinate 2 are shown as dotted lines. All units are dimensionless.

nal weighting matrices. P_{Vj} and W_{Vj} are cost function weighting factors and Γ_i are normalized weights on initial conditions. The subscript i sums over each trajectory and j sums over each element of the state. This cost functional differs from that of (3.13) in that there is no Heaviside function weighting the final momentum and in that the integral term weights against values of the average position and momentum different from zero instead of weighting against displacement from initial conditions.

The first ensemble of initial conditions studied were 16 values of q_1 and q_2 centered about $q_1=-1$, $q_2=1$ with both momenta taken as zero. Results for integrating these initial conditions with zero external field are shown for $k=0.4$ in Fig. 4 and for $k=0.6$ in Fig. 5. For the $k=0.4$ case, the trajectories have dispersed and fill the diagonal region between $(q_1=-1,\ q_2=1)$ and $(q_1=1,\ q_2=-1)$ fairly evenly but have not explored outside this region by $t=8\pi$. It is seen in Fig. 5, that some trajectories have broken free of the diagonal region for the $k=0.6$ case by $t=8\pi$. The decay of peak mean values of displacement and momentum in Figs. 4(a), 4(b), 5(a), and 5(b) is a result of trajectory spreading. Figures 4(c) and 5(c) show plots of displacement variance. The magnitude of the variance at $t=8\pi$ for $k=0.6$ is seen to be almost twice as large as that for $k=0.4$. Only one curve is shown in both Figs. 4(c) and 5(c) because symmetry in the initial conditions causes the variances of q_1 and q_2 to be equal.

Control results for $k=0.4$ are shown in Fig. 6 for $T=8\pi$, $\omega_e=1\times10^{-7}$, $\gamma_2=-1$, $P_{f2,2}=1$, and all other weights zero. Figure 6(a) shows the driving field, which has a rough periodicity of about 2π. Figure 6(b) shows that $\bar{q}_2$ reaches the desired value -1 at $t=T$, with the peak amplitudes of both q_1 and q_2 close to 1 during the entire interval. However, Fig. 6(c), a plot of displacement variance, and Fig. 6(d), the trajectories at $T=8\pi$, show that there is a fair amount of spread in the trajectories at the target time. Nevertheless, a comparison of Figs. 4(e) and 6(d) shows that the controlled case results in most of the trajectories being bundled together near the target value of γ_2. The field has reduced the variance over that of the uncontrolled case shown in Fig. 4(c). A comparison of $\bar{q}_2$ in Figs. 4(a) and 6(b) shows that the field primarily introduces a frequency shift to meet its target objective.

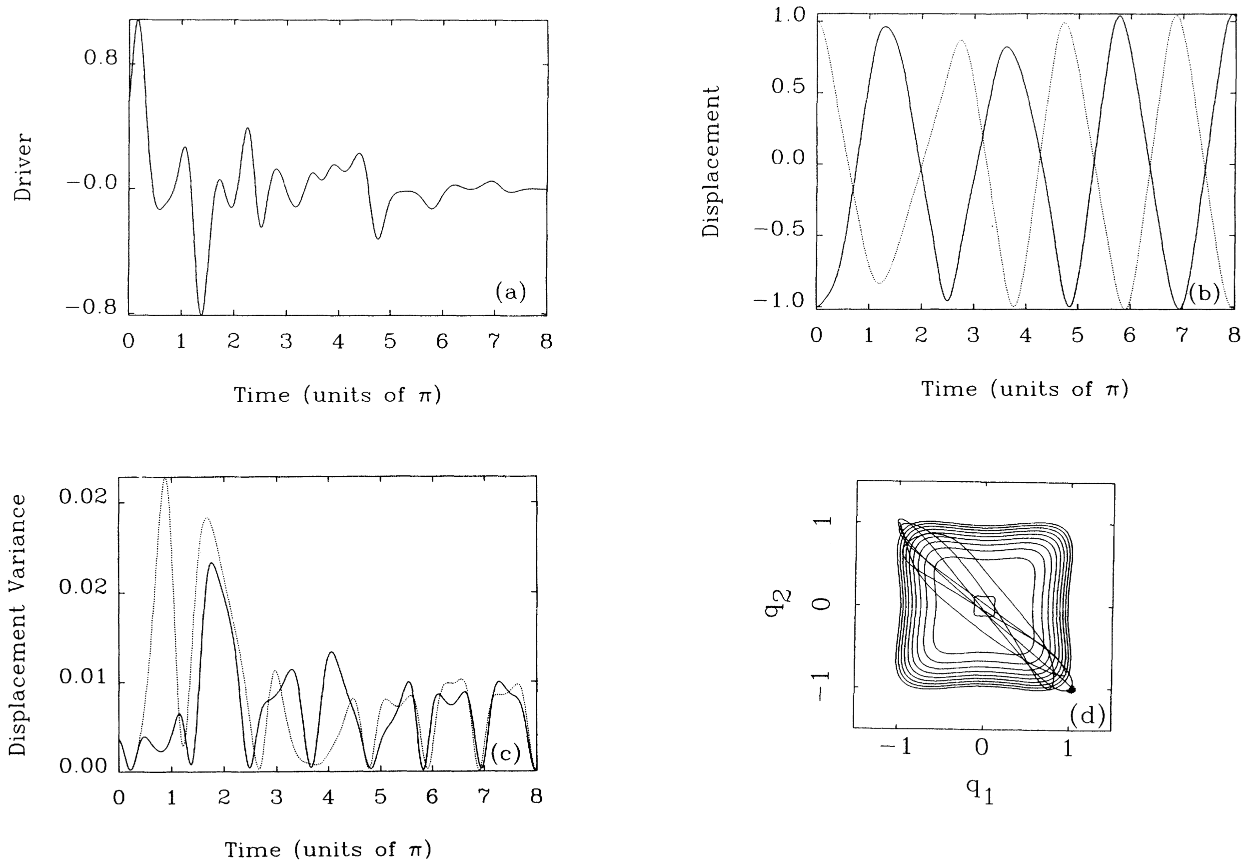

FIG. 7. Optimal control results for the system shown in Fig. 4 with variance control: (a) optimal field, (b) displacement, (c) displacement variance, and (d) the trajectories at the final time, with the average path shown as a solid curve. The objective of stretching $\bar{q}_2$ to 1 was met with less spreading than in Fig. 6. Properties of coordinate 1 are shown as solid lines and those of coordinate 2 are shown as dotted lines. All units are dimensionless.

Figure 7 shows that the trajectory spread can be reduced further if, in the variance part of the cost functional, we set $W_{V1}=W_{V2}=1$, the rest being the same. $\bar{q}_2(T)$ still reaches its target of -1, as seen in Fig. 7(b), but the variance of the bundle of trajectories is now much lower, as seen in Fig. 7(d), in comparison with Fig. 6(d). The curve in Fig. 7(d) depicts the average path taken by the ensemble and shows that only a relatively narrow region of position space is sampled during the control interval. The trade-off for low variance is a field with much high complexity and larger peak amplitude as seen in Fig. 7(a).

There results are encouraging so far, but what if we explore a region where there is more chaos? Figures 8 and 9 show results for cases analogous to those in Figs. 6 and 7 but where $k=0.6$. Figure 8(a) shows the driving field for the cost functional weighting primarily the demand that $\bar{q}_2(T)=-1$ ($T=8\pi$, $\omega_e=1\times10^{-7}$, $\gamma_2=-1$, $P_{f2,2}=1$). This field is more complicated than that in Fig. 6(a), and its peak magnitude is about twice as great. Figure 8(b) shows that the objective of stretching q_2 to -1 at $t=T$ has been satisfactorily achieved, but the spread is large, as demonstrated by Figs. 8(c) and 8(d). Figure 8(c) shows a peak variance more than two times as large as that in Fig. 6(c), and this is corroborated by Figs. 8(d), showing the large spread in the positions of the 16 trajectories at the final time. The actual values of the displacement averages and variances cannot be ascertained from the trajectory plots because the trajectories are weighted by the Wigner distribution determined from the initial conditions. Therefore, casual inspection of Fig. 8(d) is somewhat misleading with respect to the value of $\bar{q}_2(T)$.

Figure 9 shows that even in this highly chaotic system, the spread of tightly bunched initial conditions can be controlled to a very high degree even by a driver with very restricted allowed interaction. Here the cost functional is the same as for the results in Fig. 8, but with two variance terms weighted: $W_{V1}=W_{V2}=1$. Figure 9(a) shows the driver, which now has a peak magnitude of about six times that seen in Fig. 8(a). The large peak at the beginning of the control fields in Figs. 7(a) and 9(a) suggests that variance reduction is enhanced if the ensemble is initially "imprinted" by the driver. Figure 9(b) shows that $\bar{q}_2(T)$ is close to its preordained value of -1, but the time histories of $\bar{q}_1(t)$ and $\bar{q}_2(t)$ are quite different from those in Fig. 8(b), in contrast to the difference be-

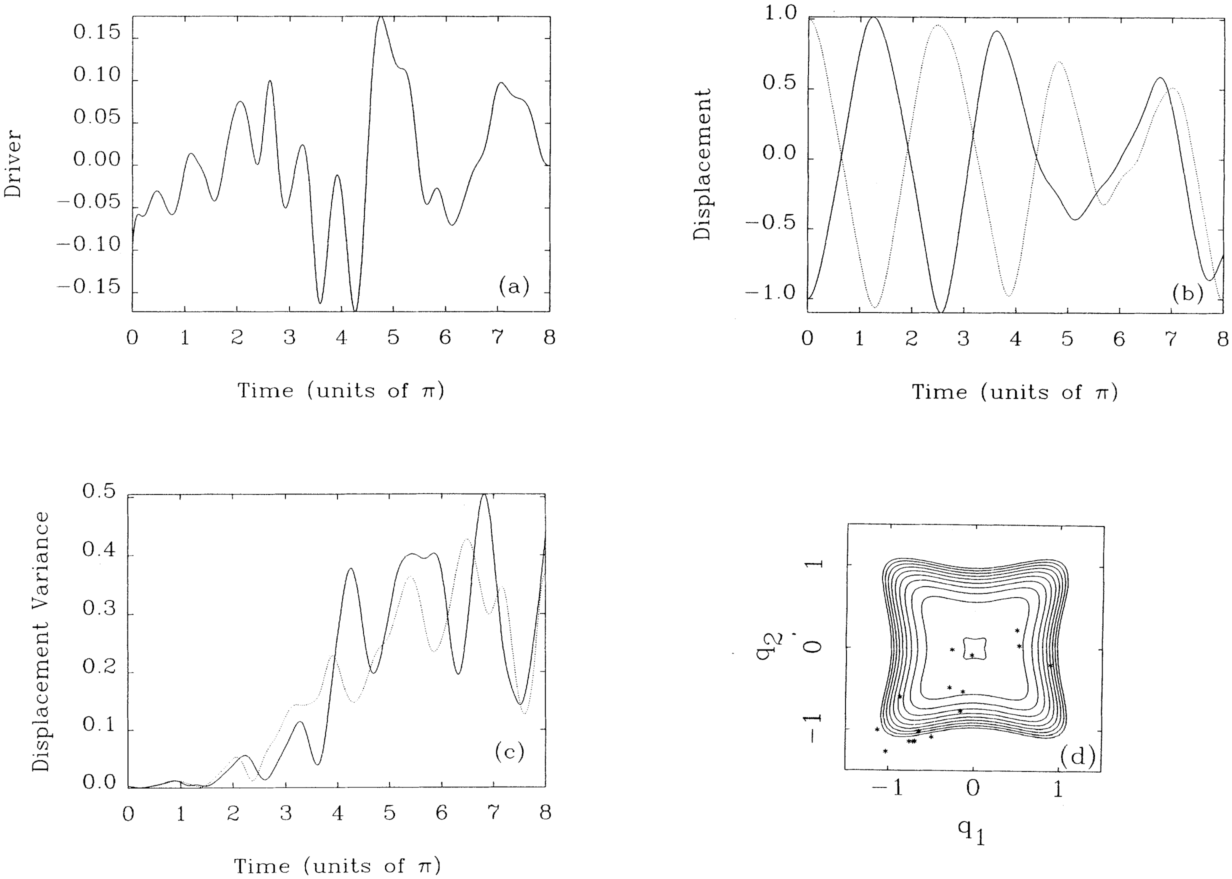

FIG. 8. Optimal control results for the system shown in Fig. 5 with no variance control: (a) optimal field, (b) displacement, (c) displacement variance, and (d) the trajectories at the final time. Properties of coordinate 1 are shown as solid lines and those of coordinate 2 are shown as dotted lines. All units are dimensionless.

tween Figs. 6(b) and 7(b). The peak variance for this case is seen in Fig. 9(c) to be about a factor of 5 smaller than that in Fig. 8(c). This reduction in spread can be seen at the final time by comparing Figs. 8(d) and 9(e). In Fig. 9(e) most trajectories are relatively closely bunched at the target time with a few exceptions, while the trajectories are widely spread in Fig. 8(d). A trace of the average position of the ensemble throughout the control interval in Fig. 9(e) shows that more regions of position space are sampled here than for the case shown in Fig. 7(d). Figure 9(d) is a plot of $H_0(t)$ of the system during the control interval. It illustrates part of the scheme by which variance is reduced: the large initial pulse of the driver draws energy out of the system so that less phase space is available to spread into. Then, at $t=7\pi$, the energy is pumped back up so that the final objective can be reached. This behavior shows, once again, how the optimal control formalism takes advantage of dynamical features to best

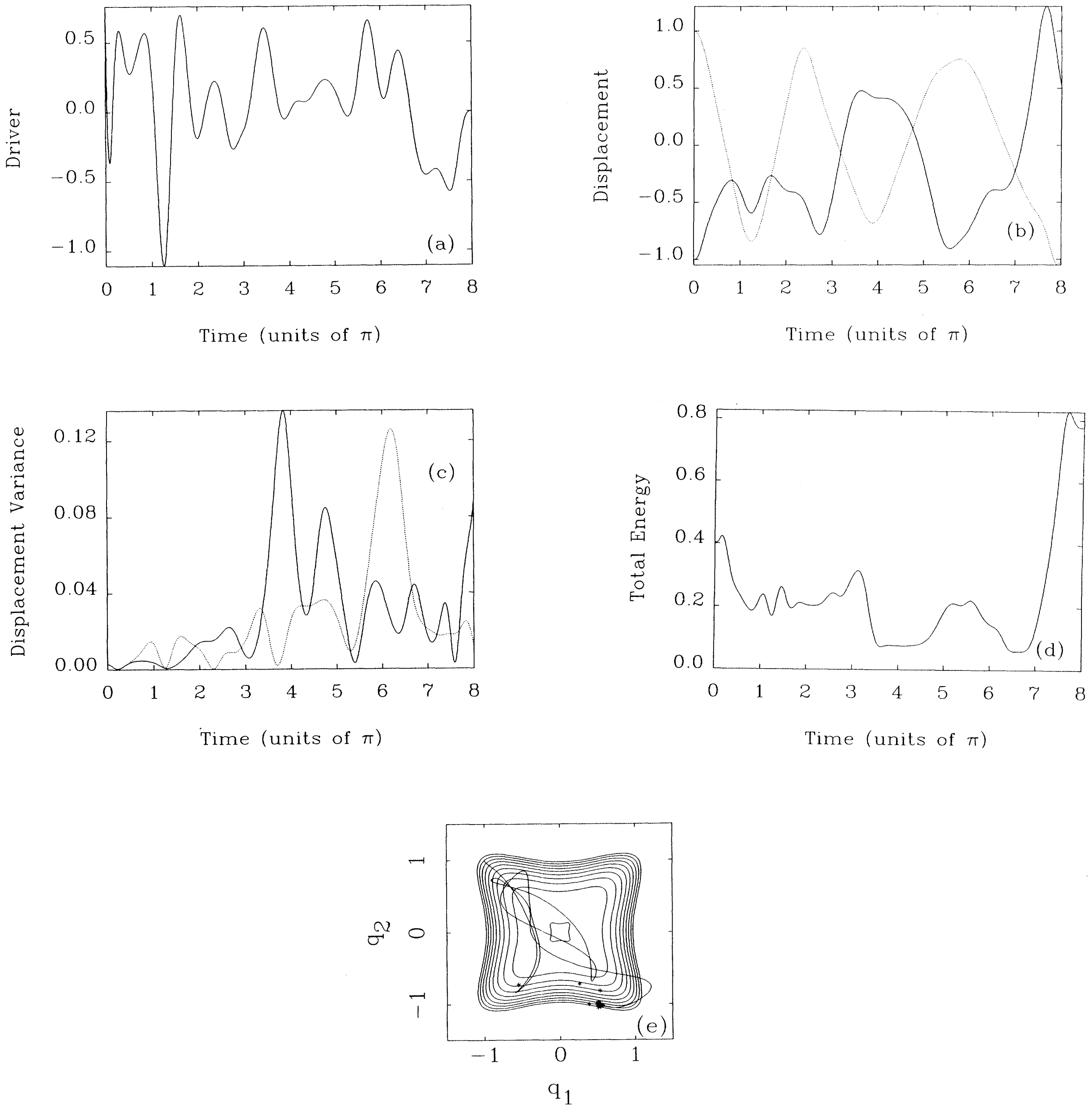

FIG. 9. Optimal control results for the system shown in Fig. 5 with variance control: (a) optimal field, (b) displacement, (c) displacement variance, (d) total energy of the system (excluding driver interaction), and (e) the trajectories at the final time, with the average path of the 14 most closely bunched trajectories shown as a solid curve. Properties of coordinate 1 are shown as solid lines and those of coordinate 2 are shown as dotted lines. All units are dimensionless.

achieve chosen objectives.

The second set of initial conditions we used was 25 trajectories clustered around ($q_1=0.1$, $q_2=0.1$). The target in these calculations was to stretch $q_2(T)$ to 1 with $q_1(T)$ not specified. Results for $k=0.6$ are shown in Figs. 10 and 11. Figure 10 contains results for $T=8\pi$, $\omega_e=1\times10^{-7}$, $P_{f2,2}=1$, and all other weights zero. Figure 10(a) shows the driving field, which has low amplitude until $t\approx5\pi$, when strong pumping commences. The field drops to zero before the final time because the target stretch q_2 is not directly pumped by the field, and similar behavior is found in all the other cases studied here. Figure 10(b) shows the displacement of the two degrees of freedom. It is seen that, although $\bar{q}_2(T)$ does reach the target of 1, its peak magnitude is at a slightly earlier time and the peak magnitude of $\bar{q}_1$ is greater at about -1.2. Figure 10(c) shows a large variance in q_2 near $t=8\pi$ and this is corroborated by Fig. 10(d), which shows a significant bifurcated spread in the trajectories at the target time. The average trajectories of the two separated bundles of trajectories are shown in Fig. 10(d). Weights of 1 were then placed on the integral variances of q_1 and q_2 and the results are shown in Fig. 11. Figure 11(a) shows that, although the final 2π of the pulse is similar to that of the field in Fig. 10(a), the field in Fig. 11(a) shows higher amplitude at earlier times. Displacements $q_1(t)$ and $q_2(t)$ in Fig. 11(b) are similar to those in Fig. 10(b). Figure 11(c) shows that the peak variance of q_2 has been reduced by a factor of 4 from the previous case, and Fig. 11(d) shows that all the trajectories are tightly bunched, except for one on the opposite side of the potential well. This errant trajectory is weighted very little in the cost functional because it originates from an outlying region of the initial Wigner distribution and, hence, makes only a small contribution to the average displacements or variances. The same comment applies to the few errant trajectories in Fig. 9(e). The paths of the two separate bundles are also shown in Fig. 11(d). It is seen that since pumping only occurs in the q_1 direction, the trajectories must ricochet off the convex potential surface after they have achieved enough energy to reach their objective in order to pump the q_2 degree of freedom.

It should be noted that we chose difficult objectives for the example cases. The control objectives involved $\bar{q}_2$ ex-

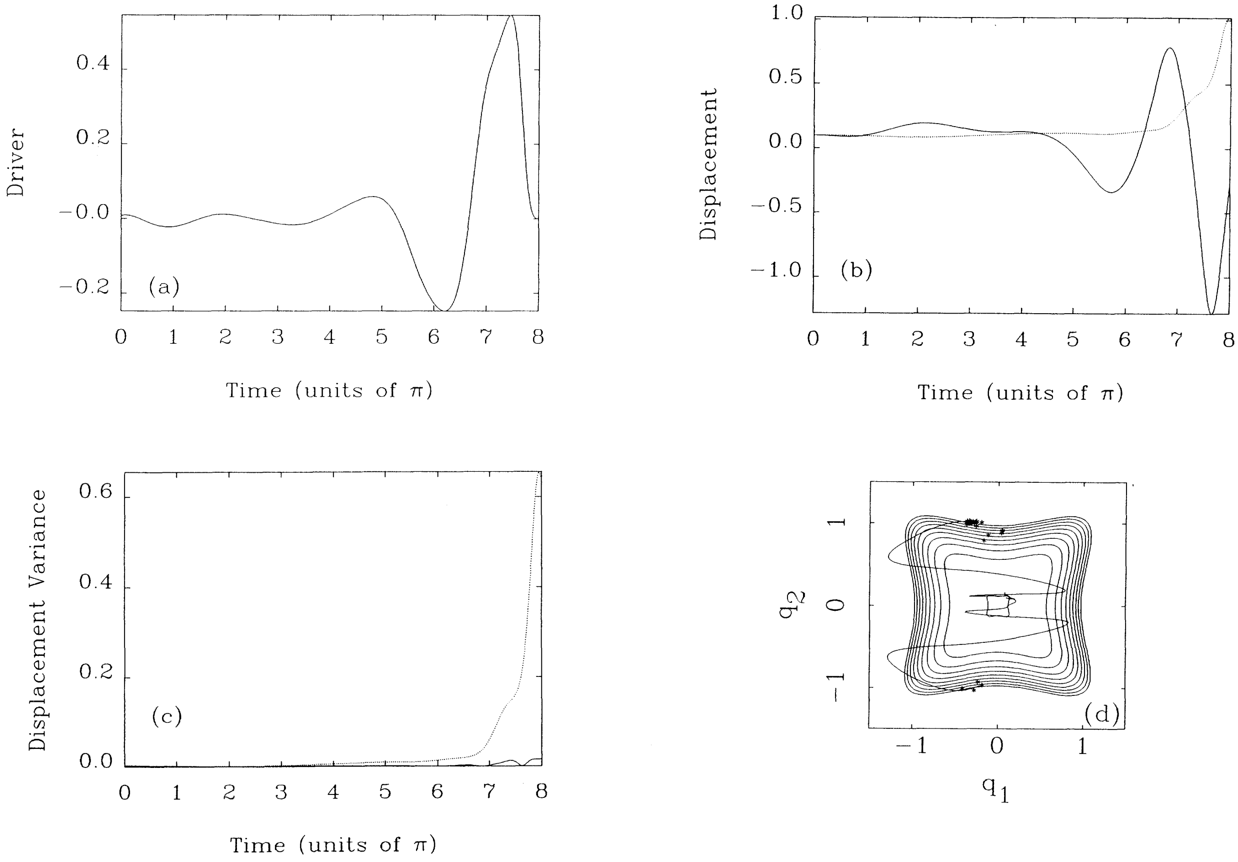

FIG. 10. Results for attempting to stretch $q_2(T)=1$ from a low-energy initial state with no variance control using $k=0.6$: (a) optimal field, (b) displacement, (c) displacement variance, and (d) the trajectories at the final time, with the average paths of both trajectory bundles shown as solid curves. Properties of coordinate 1 are shown as solid lines and those of coordinate 2 are shown as dotted lines. All units are dimensionless.

clusively, while the control term only directly acted on q_1. Control was accomplished by the field working in a complex but cooperative fashion with the dynamical capabilities of the system. Thus, a rather surprising degree of control was achieved in this chaotic system even with a highly constrained control.

On a more sober note, the control results for the sample cases shown in Figs. 8 and 9 took an enormous amount of computer time for this relatively-modest-sized problem (only 16 trajectories). It was seen that at most points in field space during the search for a minimum, the gradient pointed downhill for a very small interval, at which point the direction of a new gradient had to be calculated. Because the step size at each iteration was small, many iterations had to be taken to reach an acceptable minimum. This behavior suggests that the cost hypersurface is quite convoluted and that gradient searches may be an inefficient method of finding even local minima. Other search methods such as simulated annealing may be more appropriate for such problems.

Comparison of Figs. 10 and 11 shows that relatively small changes in the electric field can cause large differences in the dynamics of the system. However, it is important that the objective not be very sensitive to the electric-field variations because inevitable small errors made in real laboratory fields would be likely to cause undesired results. It is possible to include terms in the cost functional that add in robustness requirements to achieving system objectives in the face of driving field errors. Robustness to uncertainty in system parameters is also important, and preliminary results using sensitivity minimization [2] and averaging over the uncertain parameters [21] have already been studied.

V. SUMMARY

We have shown that optimal control theory can be used to design fields to achieve a molecular objective in the classical regime. The use of classical mechanics is important because if any molecule larger than a triatomic outside of the harmonic regime is to be controlled, the equations of motion must be classical. Also, initial guesses for an expensive full quantum calculation could be generated by using the classical mechanical analog first.

It was seen that it is possible to design fields that lead

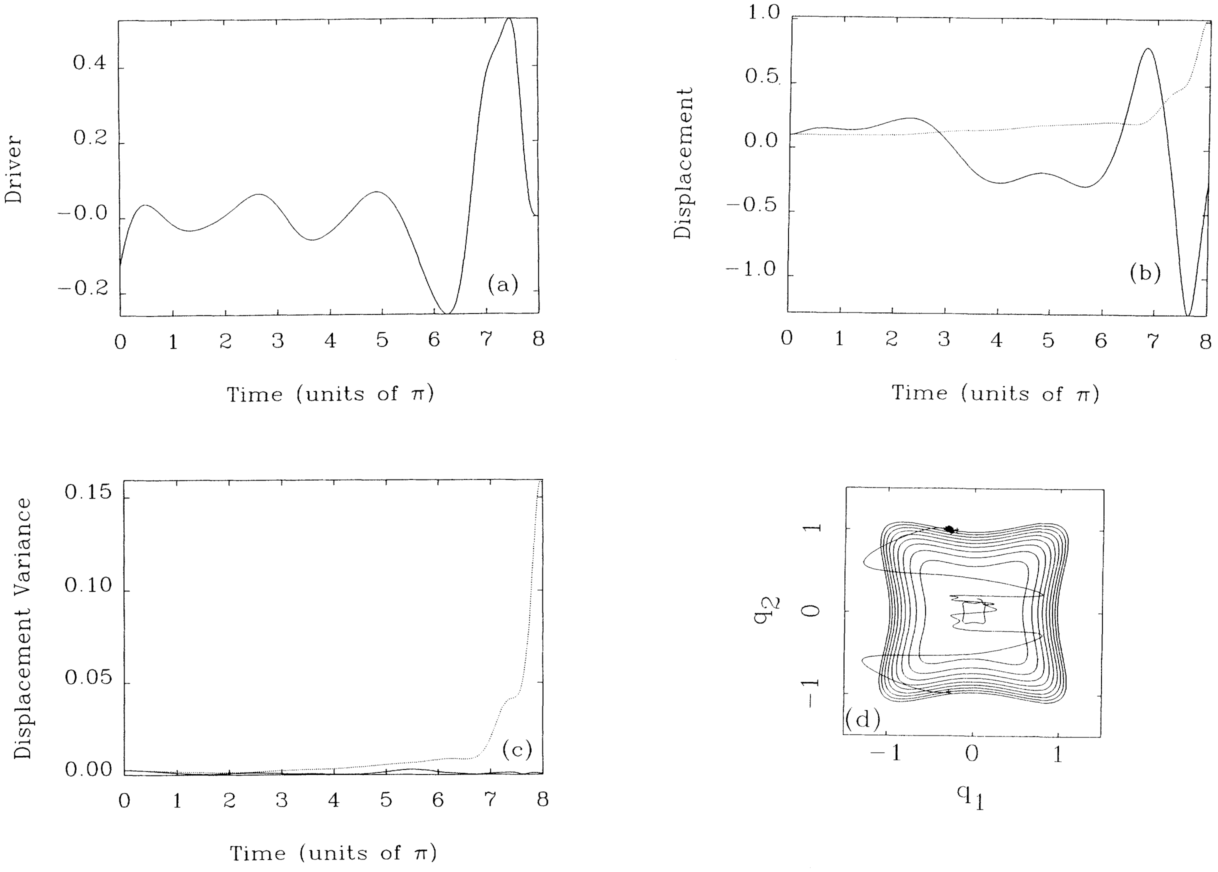

FIG. 11. Results for attempting to stretch $q_2(T)=1$ from a low-energy initial state with variance control using $k=0.6$: (a) optimal field, (b) displacement, (c) displacement variance, and (d) the trajectories at the final time, with the average paths of both trajectory bundles shown as solid curves. Properties of coordinate 1 are shown as solid lines and those of coordinate 2 are shown as dotted lines. All units are dimensionless.

to large branching ratios ($>95\%$) in the desired exit channel for total energies that cause the molecule to exit a lower energy channel if the dynamics were statistical. However, in order to achieve bond breaking on the short-time scales used in this study, strong fields must be generated. These are not yet practical experimentally and may require the inclusion of electronic effects for a proper molecular description. The peak amplitudes could be reduced by lengthening the control interval and changing L_2. For sufficiently long pulses, rotational motion must also be included.

We demonstrated control over systems exhibiting dynamical chaos, but problems may arise if control intervals are greatly increased. Other systems should be studied to see if regions of phase space exhibiting chaos can be avoided by using a carefully chosen cost functional. Even when chaos is not present, the issue of classical versus quantum behavior is an important matter. To assure that a given field produces the same physical results both quantum mechanically and classically, it is possible to include both descriptions in a cost functional demanding that selected corresponding expectation values be equal. These enhanced tasks certainly pose important challenges in the molecular control domain. The present paper serves to illustrate the capability of approaching these problems in a classical mechanical context.

ACKNOWLEDGMENTS

Special thanks to Dr. Shenghua Shi for providing data for the quantum comparison and to Professor Kevin Lehmann for suggesting the form of the quartic-oscillator Hamiltonian. The authors acknowledge support for this research from the Army Research Office and the Office of Naval Research.

---

[1] S. Shi, A. Woody, and H. Rabitz, J. Chem. Phys. **88**, 6870 (1988).
[2] C. Schwieters, J. G. B. Beumee, and H. Rabitz, J. Opt. Soc. Am. B **7**, 1736 (1990).
[3] J. G. B. Beumee and H. Rabitz, J. Math. Phys. **31**, 1253 (1990).
[4] S. Shi and H. Rabitz, Chem. Phys. **139**, 185 (1989).
[5] S. Shi and H. Rabitz, J. Chem. Phys. **92**, 364 (1990).
[6] S. Shi and H. Rabitz, Comput. Phys. Commun. **63**, 71 (1991).
[7] A. Peirce, M. Dahleh, and H. Rabitz, Phys. Rev. A **37**, 4950 (1988).
[8] R. Judson, K. K. Lehmann, W. S. Warren, and H. A. Rabitz, J. Mol. Struct. **223**, 425 (1990).
[9] D. J. Tannor and S. A. Rice, J. Chem. Phys. **83**, 5013 (1985); S. A. Rice, D. J. Tannor, and R. Kosloff, J. Chem. Soc. Faraday Trans. 2 **82**, 2423 (1986); R. Kosloff, S. A. Rice, P. Gaspard, S. Tersigni, and D. J. Tannor, Chem. Phys. **139**, 201 (1989); S. H. Tersigni, P. Gaspard, and S. A. Rice, J. Chem. Phys. **93**, 1670 (1990).
[10] R. Walker and R. Preston, J. Chem. Phys. **67**, 2017 (1977).
[11] K. C. Kulander and A. E. Orel, J. Chem. Phys. **75**, 675 (1981).
[12] M. J. Davis and E. J. Heller, J. Chem. Phys. **80**, 5036 (1984).
[13] T. B. Fowler, IEEE Trans. Auto. Cont. **34**, 201 (1989).
[14] A. Hübler, Helv. Phys. Acta **62**, 343 (1989).
[15] E. Ott, C. Grebogi, and J. A. Yorke, Phys. Rev. Lett. **64**, 1196 (1990).
[16] E. B. Wilson, Jr., J. C. Decius, and P. C. Cross, *Molecular Vibrations* (Dover, New York, 1980).
[17] E. Wigner, Phys. Rev. **40**, 749 (1932).
[18] H.-D. Meyer, J. Chem. Phys. **84**, 3147 (1986).
[19] I. C. Percival and A. Carnegie, J. Phys. A **17**, 801 (1984).
[20] M. Hénon and C. Heiles, Astron. J. **69**, 73 (1964).
[21] M. Dahleh, A. P. Peirce, and H. Rabitz, Phys. Rev. A **42**, 1065 (1990).